CANCER

Critical role of lncEPAT in coupling dysregulated EGFR pathway and histone H2A deubiquitination during glioblastoma tumorigenesis

Linlin Li[1]†, Aidong Zhou[2]†, Yanjun Wei[3], Feng Liu[4], Peng Li[1], Runping Fang[1], Li Ma[2], Sicong Zhang[5], Longqiang Wang[2], Jinze Liu[6,7], Hope T. Richard[7,8], Yiwen Chen[3,9], Hengbin Wang[7,10], Suyun Huang[1,7,11]*

Histone 2A (H2A) monoubiquitination is a fundamental epigenetics mechanism of gene expression, which plays a critical role in regulating cell fate. However, it is unknown if H2A ubiquitination is involved in EGFR-driven tumorigenesis. In the current study, we have characterized a previously unidentified oncogenic lncRNA (lncEPAT) that mediates the integration of the dysregulated EGFR pathway with H2A deubiquitination in tumorigenesis. LncEPAT was induced by the EGFR pathway, and high-level lncEPAT expression positively correlated with the glioma grade and predicted poor survival of glioma patients. Mass spectrometry analyses revealed that lncEPAT specifically interacted with deubiquitinase USP16. LncEPAT inhibited USP16's recruitment to chromatin, thereby blocking USP16-mediated H2A deubiquitination and repressing target gene expression, including *CDKN1A* and *CLUSTERIN*. Depletion of lncEPAT promoted USP16-induced cell cycle arrest and cellular senescence, and then repressed GBM cell tumorigenesis. Thus, the EGFR-lncEPAT-ubH2A coupling represents a previously unidentified mechanism for epigenetic gene regulation and senescence resistance during GBM tumorigenesis.

INTRODUCTION

Glioblastoma (GBM), accounting for more than 60% of all newly diagnosed glioma cases, is the most malignant and devastating form of glioma and is virtually incurable (*1*). Epidermal growth factor receptor (EGFR) signaling is constitutively activated in most GBM due to aberrations in EGFR and its ligands such as EGF and transforming growth factor α (TGFα) (*2*, *3*). Over 50% of human GBMs show amplification or overexpression of EGFR, and half of EGFR-amplified tumors express the mutant receptor EGFRvIII, which causes constitutive activation of the receptor in a ligand-independent manner (*4*). Dysregulated EGFR signaling confers a poor prognosis and resistance to traditional therapies in GBM patients; thus, targeting EGFR has been regarded as a promising therapeutic strategy (*5*, *6*). A few studies have shown that the EGFR pathway regulates cellular senescence, an irreversible growth arrest state in protecting organisms against cancer. Inhibition of EGFR arrests mammalian cell growth by inducing cellular senescence (*7*). Moreover, EGFR inhibitors radiosensitize non–small cell lung cancer (NSCLC) cells by triggering the senescence program (*8*). These studies suggest that the EGFR-mediated anti-senescence effect constitutes an important mechanism that facilitates tumor formation and therapy resistance, but the underlying mechanisms are largely unknown.

Histone 2A ubiquitination (ubH2A) marks chromatin at bivalent genes to control gene transcription. Histone 2A lysine-119 monoubiquitination (H2AK119ub1) is primarily catalyzed by polycomb-repressive complex 1 (PRC1), which strongly links H2AK119ub1 to tumor development (*9*–*11*). Like other histone modifications, ubH2A is a reversible marker that is removed by deubiquitinating enzymes. Thus, ubH2A levels are determined by the balance between PRC1-mediated H2A ubiquitination and ubH2A deubiquitination. Ubiquitin-specific protease 16 (USP16) is one of the main deubiquitinases that antagonize PRC1-mediated H2A mono-ubiquitination (*12*–*14*). USP16 knockout is embryonic lethal in mice because of defective $Usp16^{-/-}$ ESCs (embryonic stem cells) for differentiation (*15*). Moreover, USP16 overexpression reduces the expansion of neural progenitor cells by decreasing H2AK119 ubiquitination, which leads to a reduction in self-renewal and accelerated cellular senescence in Down syndrome (*16*). Therefore, USP16 is a key epigenetic switch that regulates stem cell self-renewal and cellular senescence. However, the mechanisms that regulate USP16's recruitment to target promoters are largely unknown.

Transcriptome profiling has identified thousands of transcripts longer than 200 nucleotides, the so-called long noncoding RNAs (lncRNAs). A small fraction of lncRNAs have been characterized as having critical roles in chromatin remodeling, gene transcription, RNA splicing and stability, or protein translation (*17*, *18*). Emerging evidence has shown that lncRNAs are frequently dysregulated in human cancers and are involved in multiple processes, including cell growth, apoptosis, invasion, and tumor metastasis (*19*, *20*).

In human GBM, little is known about whether lncRNAs are involved in EGFR-driven tumorigenesis. In this study, we identified and characterized an EGFR pathway-activated transcript (lncEPAT)

[1]Department of Human and Molecular Genetics, School of Medicine, Virginia Commonwealth University, Richmond, VA 23298, USA. [2]Department of Neurosurgery, The University of Texas MD Anderson Cancer Center, Houston, TX 77030, USA. [3]Department of Bioinformatics & Computational Biology, The University of Texas MD Anderson Cancer Center, Houston, TX 77030, USA. [4]Ludwig Institute for Cancer Research, University of California, San Diego, La Jolla, CA 92093, USA. [5]Laboratory of Biochemistry and Molecular Biology, The Rockefeller University, New York City, NY 10065, USA. [6]Department of Biostatistics, School of Medicine, Virginia Commonwealth University, Richmond, VA 23298, USA. [7]VCU Massey Cancer Center, School of Medicine, Virginia Commonwealth University, Richmond, VA 23298, USA. [8]Department of Pathology, School of Medicine, Virginia Commonwealth University, Richmond, VA 23298, USA. [9]Quantitative Sciences Program, MD Anderson Cancer Center UTHealth Graduate School of Biomedical Sciences, Houston, TX, 77030, USA. [10]Department of Internal Medicine, Division of Hematology, Oncology and Palliative Care, School of Medicine, Virginia Commonwealth University, Richmond, VA 23298, USA. [11]Virginia Commonwealth University Institute of Molecular Medicine, Richmond, VA 23298, USA.
*Corresponding author. Email: suyun.huang@vcuhealth.org
†These authors contributed equally to this work.

that is induced by dysregulated EGFR activation. We showed that lncEPAT interacted with USP16 protein and critically regulated USP16-mediated H2A deubiquitination, thereby providing new insight into the regulation of H2A ubiquitination and gene transcription by EGFR activation. Further, lncEPAT attenuated USP16-induced cellular senescence and thus promoted GBM cell growth and tumorigenesis. The results of our study suggest that targeting lncEPAT may be an effective pro-senescence therapeutic target for GBM.

RESULTS

LncEPAT is induced by dysregulated EGFR, and lncEPAT level correlates with glioma grade

To identify lncRNAs that correlate with glioma tumor grade and are involved in GBM progression, the microarray data of the Gene Expression Omnibus public datasets GSE4290 that includes 23 no-tumor samples from epilepsy patients and 157 glioma samples of different grade were analyzed for differentially expressed lncRNAs. Forty differentially expressed lncRNAs in different grades of glioma were identified while compared to no-tumor samples (Fig. 1A). We also analyzed lncRNA profile in glioma cases on The Cancer Genome Atlas database (TCGA) and in normal brain tissues from The Genotype-Tissue Expression project (GTEx) database. Five hundred and seventy-four lncRNAs were differentially expressed in different grades of glioma versus normal brain (Fig. 1A). Next, we found that eight lncRNAs (nine gene probes) overlapped in these two analyses (Fig. 1A), indicating that these eight lncRNAs overexpressed in glioma. Moreover, the levels of these eight lncRNAs correlated with the grades of glioma (Fig. 1A; fig. S1, A and B; and table S1).

Next, we examined whether these eight lncRNAs are regulated by the dysregulated EGFR pathway by using U87 parental and U87/EGFRvIII cells. Seven of the eight lncRNAs were up-regulated by >2-fold in U87/EGFRvIII cells compared with U87 parental cells (Fig. 1, B and C). Among them, a transcript from chromatin 12q13, *LOC400043* [*LINC02381*, HUGO Gene Nomenclature Committee (HGNC)–approved symbol], was highly up-regulated, by over 19-fold in U87/EGFRvIII cells determined by quantitative polymerase chain reaction (qPCR) (Fig. 1C), which was confirmed by Northern blot analysis (Fig. 1D). We also found that the data of the correlation between expressions of four of the eight lncRNAs with EGFR gene copy number are available in a TCGA glioma dataset. The data showed that the mRNA levels of three of the four lncRNAs, including LINC02381, were positively correlated with copy number gain and amplification of EGFR gene (fig. S1C). Moreover, the levels of phosphorylated EGFR at Y1173 positively correlated with lncEPAT levels in a TCGA glioma dataset (fig. S1D). We therefore designated LINC02381 as lncEPAT. Furthermore, the induction of lncEPAT by the EGFR pathway was confirmed in LN229 cells with doxycycline-inducible EGFRvIII (LN229/EGFRvIII Tet-on), as well as in EGF-treated U87/EGFR-wt cells and GSC23 cells (patient-derived GBM stem cells) (Fig. 1, E and F, and fig. S1, E to H). Because the EGFR pathway is frequently dysregulated in lung cancer (*21*), we then detected the expression of lncEPAT in 45 NSCLC specimens. LncEPAT was significantly up-regulated in NSCLC tissues compared with corresponding adjacent normal tissues (fig. S1, I and J).

EGFR pathway dysregulation remodels epigenome and transcription factor network in human GBM (*22*). To gain insight into the transcription activity of lncEPAT in GBM tumors, we analyzed the chromatin immunoprecipitation sequencing (ChIP-seq) data to profile the H3K4me1 and H3K27ac status in a set of GBM clinical samples (*22*). Of those six GBMs, four have EGFR amplification and EGFRvIII mutation, and two have elevated expression of FGFR3. As a comparison, we also analyzed H3K27ac ChIP-seq profiles from eight different normal brain regions. H3K4me1 and H3K27ac were notably enriched near the lncEPAT transcript and its neighbor gene *HOXC4* in GBM tumors (Fig. 1G), suggesting active transcription in those regions in GBMs. Moreover, H3K27ac levels near the lncEPAT transcript and *HOXC4* were substantially higher in GBM tumors in comparison to normal brains (Fig. 1G), indicating an EGFR- and FGFR3-driving expression of lncEPAT in GBM.

We evaluated a panel of cell lines and found that lncEPAT was substantially up-regulated in GBM-derived cell lines, especially in patient-derived GSCs (glioblastoma stem cells), compared with cell lines derived from lower-grade glioma and normal human astrocytes (NHAs) (Fig. 2A). The particularly high expression of lncEPAT in GSCs may be due to the sustaining activation of EGFR signaling, as cells were cultured in stem cell medium containing EGF. We next examined the subcellular localization of lncEPAT by RNA fluorescence in situ hybridization (FISH) and found that lncEPAT predominately localized in the nucleus of GBM cells (Fig. 2B). To determine the clinical significance of lncEPAT expression in malignancy grades of glioma, we performed RNA in situ hybridization assays in 11 normal brain and tumor-adjacent tissues, 56 grade I to III astrocytomas, and 62 GBMs (grade IV) (Fig. 2C, left). Immunostaining quantification and statistical analyses demonstrated that the levels of lncEPAT expression were positively correlated with the glioma grade (Fig. 2C, right). Moreover, we compared the expression of lncEPAT in different World Health Organization (WHO) grade brain tissues using a TCGA dataset, and further confirmed that lncEPAT expression positively correlated with glioma grade (Fig. 2D).

To determine the association of lncEPAT expression with clinical outcome in glioma patients, we queried TCGA (*23*), Freije (*24*), and Phillips (*25*) glioma datasets. We found that elevated lncEPAT expression was predictive of poor glioma patient prognosis (Fig. 2E). Overall, these results suggest that lncEPAT is induced by dysregulated EGFR in GBM and that high levels of lncEPAT are positively correlated with tumor grade and predictive of poor patient survival.

EGFR pathway induces lncEPAT expression through Stat3 and c-Jun

LncEPAT is a 1399–nucleotide (nt) transcript from human *Chr12q13*, downstream of the *HOXC* gene cluster (fig. S2A). To exclude the possibility that lncEPAT is transcribed together with *HOXC4* as a polycistronic RNA, we defined the transcription start site (TSS) of lncEPAT. Two TSSs were identified by 5′-rapid amplification of complementary DNA (cDNA) end (RACE) assays in both U87/EGFRvIII and GSC23 cells (fig. S2B). High levels of H3K4me1/3 were found around the TSS of lncEPAT in multiple cell lines, suggesting active transcription in this region (Fig. 3A). Further, there is no lncEPAT amplification, deletion, or mutation in human glioma on TCGA datasets.

To identify the mechanism that drives lncEPAT overexpression in human GBM, we cloned a fragment (−3000/+1) upstream of lncEPAT TSS that harbored a noncanonical TATA-box (TATTA); it showed strong activity to drive reporter gene expression compared with the reporter only control (Fig. 3A and fig. S2, A and C). Induced overexpression of EGFRvIII significantly increased the reporter gene activity (Fig. 3B). In the promoter region, two potential

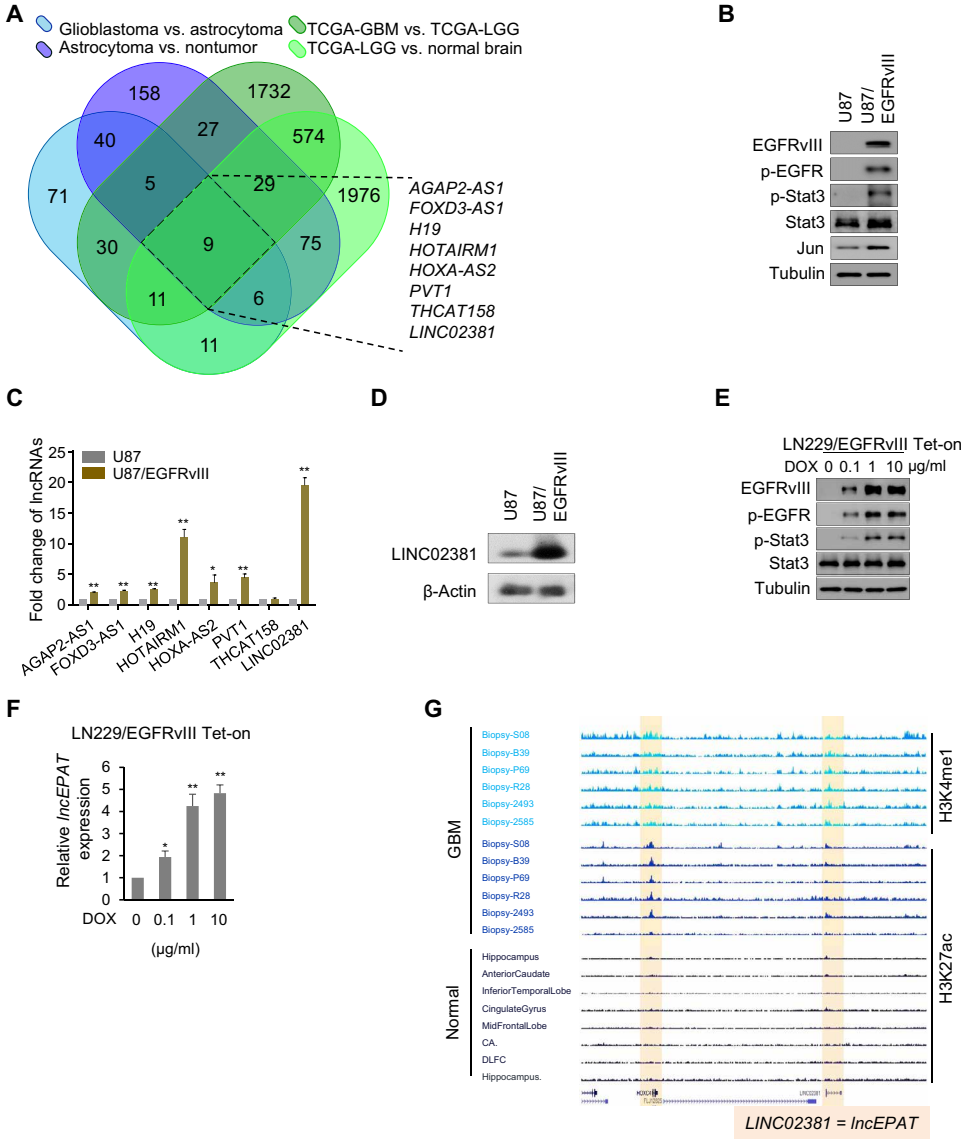

Fig. 1. LncEPAT expression is induced by the EGFR pathway and correlated with glioma grade. (**A**) Venn diagram of differentially expressed genes between different comparison groups from the GEO dataset (GSE4290), TCGA-LGG and TCGA-GBM datasets, and GTEx database. Genes were selected according to fold changes (FCs) in different comparison groups (FC > 1.5). (**B**) Cell lysates of U87 and U87/EGFRvIII were analyzed by Western blot analysis using the indicated antibodies. (**C**) Levels of the eight lncRNAs were measured by qPCR in U87 parental cells and U87/EGFRvIII cells. Values were normalized to those in U87 cells (means ± SEM, $n = 3$ independent experiments, two-tailed Student's *t* test). *HOTAIR* was used as an internal control. *$P < 0.01$ and **$P < 0.001$. (**D**) Northern blot analysis detected the expression of lncEPAT in U87 and U87/EGFRvIII cells. β-Actin was used as a loading control. (**E**) LN229/EGFRvIII Tet-on cells were treated with doxycycline (DOX) for 6 hours, and cell lysates were analyzed by Western blot analysis using the indicated antibodies. (**F**) LN229/EGFRvIII Tet-on cells were treated with doxycycline for 36 hours, and lncEPAT levels were measured by quantitative RT-PCR. *GAPDH* was used as an internal control. Data are given as means ± SEM of $n = 3$ independent experiments. *$P < 0.05$ and **$P < 0.01$, two-tailed Student's *t* test. (**G**) ChIP-seq using tissue samples, including six GBMs (four expressing high levels of EGFR and two expressing high levels of FGFR3) and eight normal brain tissues. ChIP-seq revealed H3K27ac and H3K4me1 peaks around the lncEPAT locus in GBM tissues with high levels of EGFR/FGFR3.

c-Jun binding sites and two Stat3 binding sites were predicted (Fig. 3A), and mutation of either site attenuated EGFRvIII-induced reporter gene expression (Fig. 3B). In addition, we found that c-Jun and Stat3 specifically bound to the predicated sites, and EGF treatment enhanced their binding (Fig. 3C). Moreover, EGF-induced expression of lncEPAT was attenuated by depletion of c-Jun or Stat3 (Fig. 3, D and E). In human GBMs from the TCGA dataset, the levels of c-Jun and Stat3-pY705 positively correlated with lncEPAT levels (Fig. 3, F and G). Further, inhibition of EGFR pathway activation by specific inhibitors (gefitinib and PD153035) decreased the expression levels of lncEPAT in GSCs (Fig. 3, H and I). These results indicate that dysregulated EGFR activation induces lncEPAT expression through c-Jun and Stat3 in GBM cells.

LncEPAT is essential for GBM cell proliferation and tumorigenesis

We next explored the cellular function of lncEPAT. In GBM cells, expression of lncEPAT short hairpin RNAs (shRNAs) led to decreased

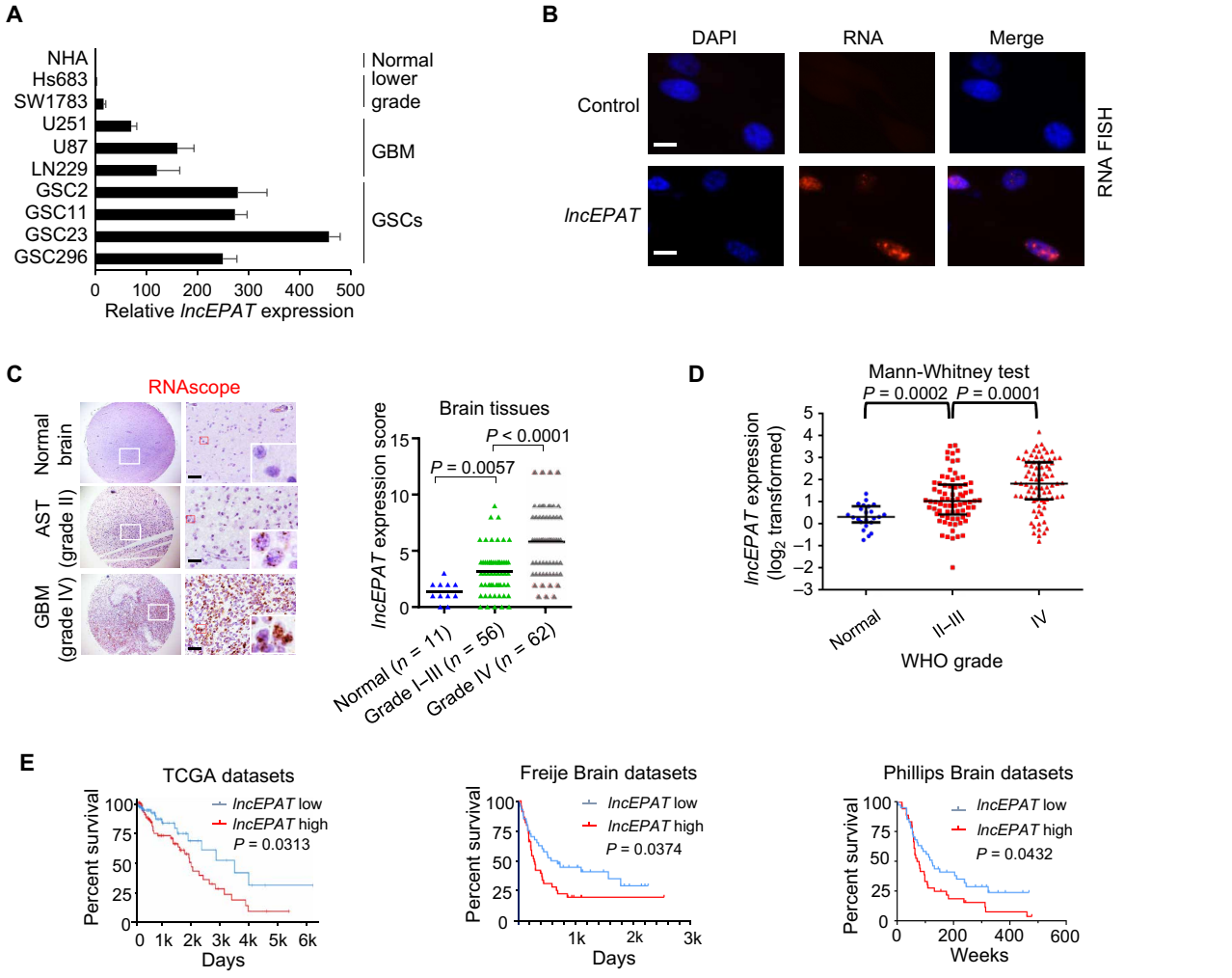

Fig. 2. LncEPAT overexpression positively correlates with glioma grade and predicts worse patient survival. (**A**) LncEPAT levels were detected by qRT-PCR in NHAs, glioma cells, and patient-derived glioma stem cells (GSCs). Data are means ± SEM of $n = 3$ independent experiments. (**B**) A FISH assay shows the localization of lncEPAT in U87/EGFRvIII cells. A probe with no endogenous complementary RNA was used as a negative control. Scale bar, 20 μm. (**C**) LncEPAT expression was examined by RNAscope assays in 11 normal brain and tumor adjacent tissues, 56 grade I to III astrocytomas, and 62 GBMs. Representative images are shown (left panel). Quantification of staining demonstrated that lncEPAT levels were positively correlated with glioma grade (right panel, normal and adjacent tissues versus grades I to III, $P = 0.0057$; grades I to III versus grade IV, $P < 0.0001$, unpaired Student's t test). (**D**) LncEPAT levels in glioma tissues of different WHO grades were analyzed using TCGA-Firehose Legacy (2016) dataset (Mann-Whitney test). (**E**) Analyses of TCGA, Freije Brain, and Phillips Brain datasets revealed that lncEPAT expression levels inversely correlated with glioma patient survival.

lncEPAT levels (Fig. 4A) and inhibited cell proliferation and anchorage-independent cell growth (Fig. 4B). Moreover, knockdown of lncEPAT inhibited neurosphere formation and cell proliferation of GSCs (Fig. 4, C and D). Furthermore, depletion of lncEPAT decreased the expression of Ki-67 in GSC23 cells (Fig. 4E).

Using an in vivo GBM mouse model, we explored the role of lncEPAT in GBM tumorigenesis. All mice injected with GSC23 and U87/EGFRvIII control cells formed tumors with characteristic GBM features (Fig. 4F, upper panel). In contrast, depletion of lncEPAT using two independent shRNAs in these cells significantly decreased the size of brain tumors (Fig. 4F, lower panel). Depletion of lncEPAT also led to decreased expression of Ki-67 and PCNA in the tumors (Fig. 4G). We next assessed the effect of lncEPAT knockdown on the survival of GBM-bearing mice. Compared with controls, depletion of lncEPAT significantly improved the overall survival of both U87/EGFRvIII-bearing (Fig. 4H, upper panel; 23 days in sh-Ctrl versus 34 days in sh1 and 39 days in sh2) and GSC23-bearing mice (Fig. 4H, lower panel; 71.5 days in sh-Ctrl versus 100.5 days in sh1 and 111 days in sh2). These results indicate that elevated expression of lncEPAT is required for cell proliferation and glioma tumorigenesis.

LncEPAT binds to USP16 and blocks USP16-mediated H2A deubiquitination

To gain insight into the functional mechanism of lncEPAT in GBM cell growth and tumorigenesis, we sought to identify the proteins associated with lncEPAT by mass spectrometry (MS) analysis. Biotinylated full-length lncEPAT or antisense transcript (AS-lncEPAT, as a control) was transcribed in vitro and incubated with GSC23 nuclear extracts. The RNA-protein complexes were purified with streptavidin-agarose beads and resolved on SDS–polyacrylamide gel electrophoresis (SDS-PAGE) electrophoresis, and specific protein

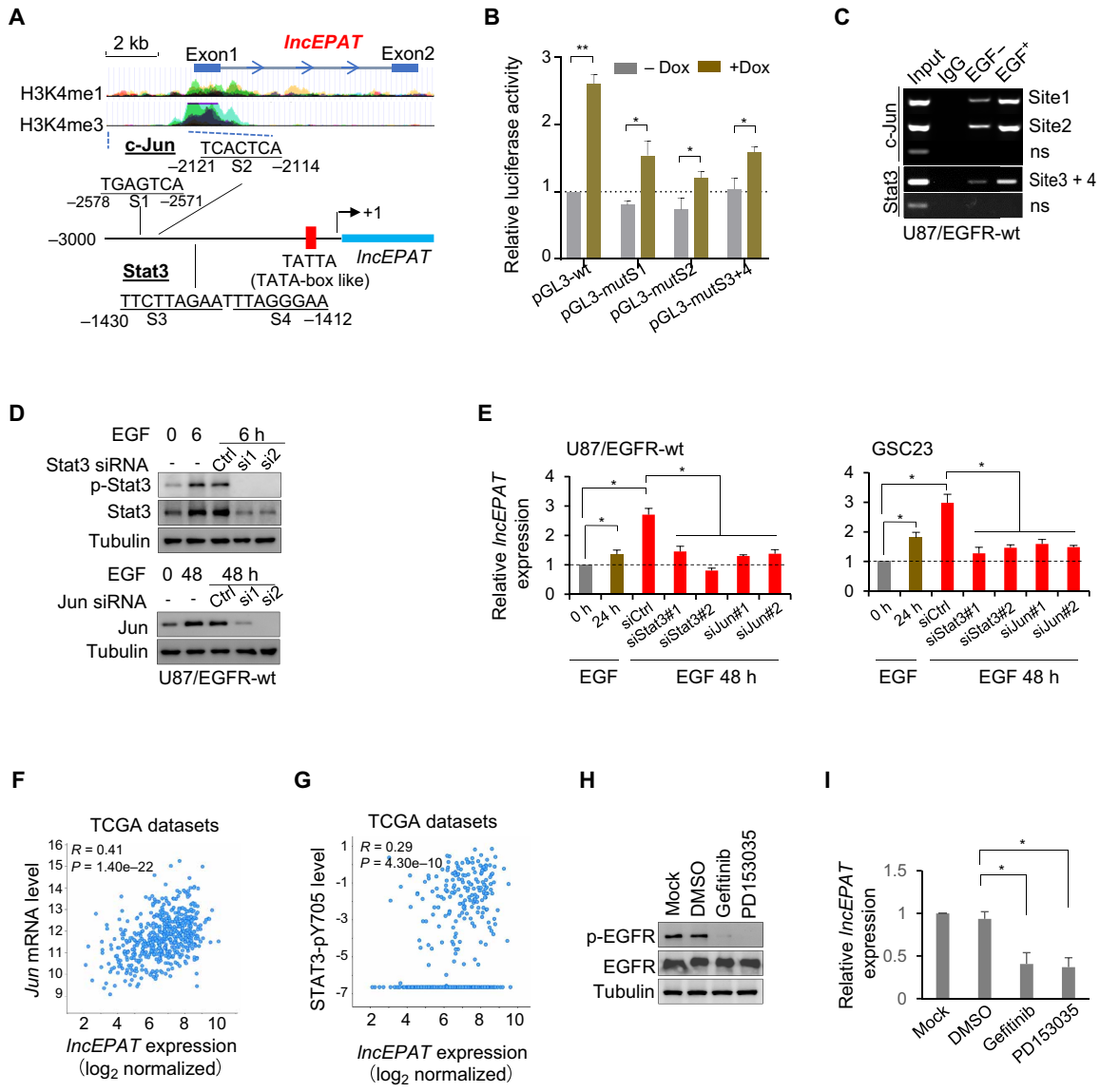

Fig. 3. EGFR pathway induces lncEPAT expression through Stat3 and c-Jun. (**A**) A diagram shows the genome and promoter region of lncEPAT, including c-Jun binding sites S1 (site 1) and S2 (site 2) and Stat3 binding sites S3 (site 3) and S4 (site 4). (**B**) Reporter luciferase activity in LN229/EGFRvIII Tet-on cells transfected with pGL3-wt, pGL3-m1 (S1 mutant), pGL3-m2 (S2 mutant), or pGL3-m3 + m4 (S3 plus S4 mutant) and then treated with doxycycline (10 μg/ml) for 36 hours. *$P < 0.05$ and **$P < 0.01$ using a two-way ANOVA test. (**C**) ChIP–semiquantitative PCR detected the binding of Stat3 and c-Jun to lncEPAT promoter in U87/EGFR-wt cells treated with EGF (50 ng/ml). ns: the lncEPAT coding region. (**D**) Western blotting of U87/EGFR-wt cells transfected with Stat3 or c-Jun siRNAs and then treated with EGF (50 ng/ml). (**E**) U87/EGFR-wt and GSC23 cells were transfected with Stat3 or c-Jun siRNAs. U87/EGFR-wt and GSC23 cells were serum-starved or deprived of EGF for 24 hours, respectively, and then treated with EGF (50 ng/ml). *$P < 0.05$, two-tailed Student's *t* test. (**F** and **G**) The correlation between the level of c-Jun or p-Stat3 (Y705) with lncEPAT level was analyzed using the TCGA dataset (Firehose Legacy, 2016). (**H**) Western blotting of p-EGFR in GSC23 cells treated with gefitinib (10 μM) or PD153035 (1.0 μM) for 6 hours. (**I**) LncEPAT expression was assessed in GSC23 cells treated with gefitinib (10 μM) or PD153035 (1.0 μM) for 48 hours. *$P < 0.05$, two-tailed Student's *t* test. Data in (B), (E), and (I) are means ± SEM from three independent experiments.

bands as identified by silver staining were subjected to MS analysis (Fig. 5A). As compared with AS-lncEPAT, lncEPAT was found to be an interacting partner with USP16, NCL, RBM10, GANAB, HSPH1, PDE4D, OSBPL9, EIF4B, CUL3, CCDC180, EFCAB13, KIF1A, and DNM3 proteins in this analysis (Fig. 5B and table S2). USP16, an ubiquitin-specific protease that was shown to deubiquitinate histone H2A (*13*), has the highest interacting score among the proteins in the MS analysis (table S2). Next, we screened the candidate lncEPAT-binding partners by the following criteria: (i) nuclear location since lncEPAT is in nucleus, (ii) possible RNA binging regions, and (iii) a direct role in cell growth. To this end, USP16 was chosen because it satisfied all the three criteria. The lncEPAT pull-down protein samples were further analyzed by Western blot analysis that showed strong staining of USP16, but not MYSM1, another H2A deubiquitinase, in both LN229 and GSC23 cells (Fig. 5C). Moreover, RNA immunoprecipitation (RIP) assays using USP16 antibody combined with reverse transcription PCR (RT-PCR) assays further confirmed the interaction between lncEPAT and USP16 (Fig. 5D).

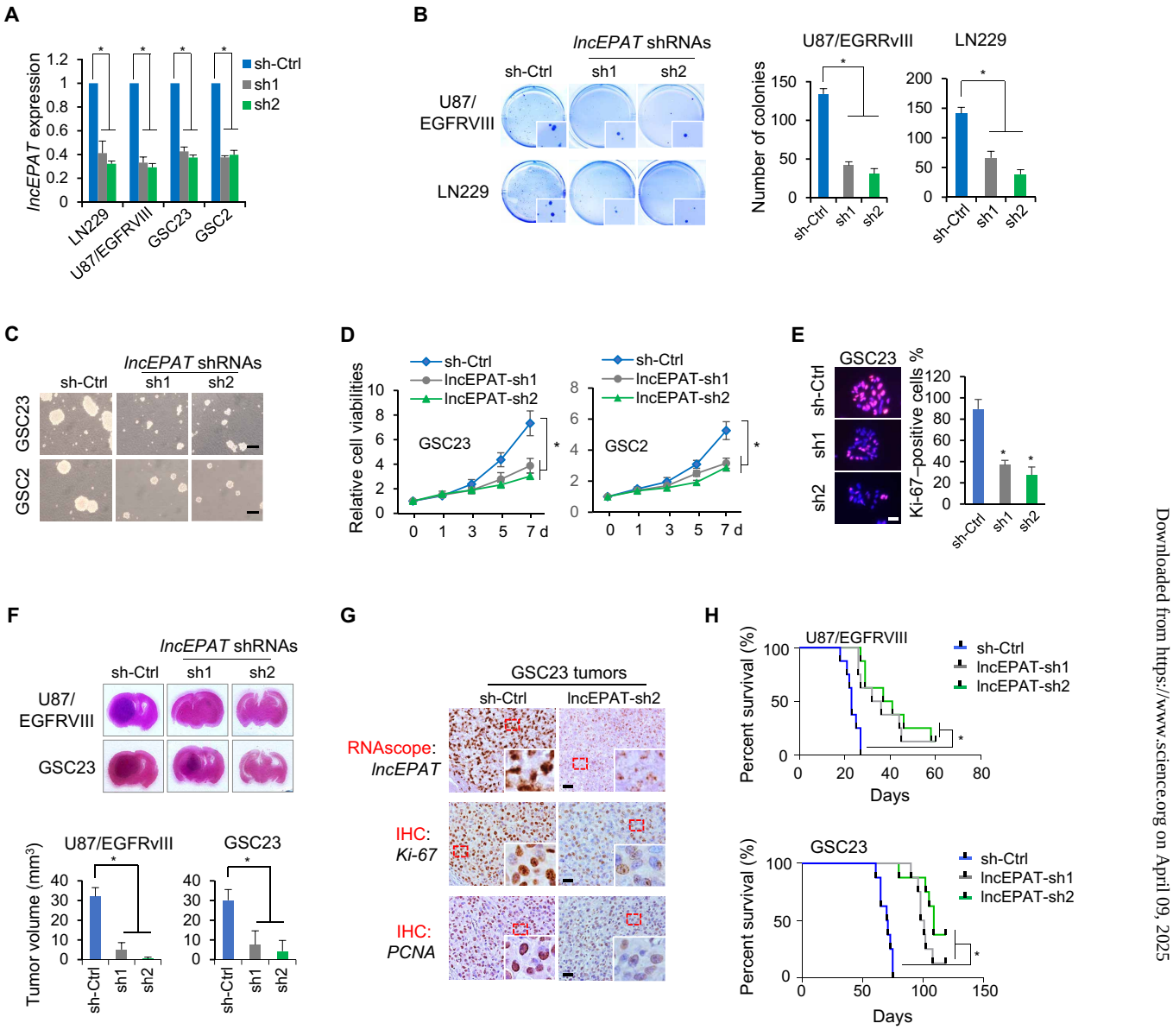

Fig. 4. LncEPAT is essential for GBM cell proliferation and tumorigenesis. (**A**) LncEPAT expression in GBM shRNA cells was measured by qRT-PCR. *$P < 0.01$, two-tailed Student's *t* test. (**B**) Colony formation of U87/EGFRvIII and LN229 shRNA cells (left panel). The number of colonies in each well was counted (right panel). *$P < 0.05$, two-tailed Student's *t* test. (**C**) Primary neurosphere formation was assessed in GSC23 and GSC2 shlncEPAT cells. Representative images are shown. Scale bar, 200 μm. (**D**) The proliferation of GSC23 and GSC2 cells with shlncEPAT was assessed by XTT. *$P < 0.05$, two-tailed Student's *t* test. (**E**) GSC23 shRNA cells were stained by Ki-67. Left panel, representative images. Right panel, representative quantification of Ki-67–positive cells in one of the three independent experiments (means ± SD of $n = 6$ randomly selected microscope fields; *$P < 0.001$, two-tailed Student's *t* test). (**F**) U87/EGFRvIII, GSC23 sh-Ctrl, or shlncEPAT cells (5×10^5 cells per mouse) were intracranially injected into nude mice. Three weeks after U87/EGFRvIII cell injection and 10 weeks after GSC23 cell injection, the brains of mice were examined. The H&E-stained sections show representative tumors (upper panel). Tumor volumes were calculated (means ± SD, $n = 8$ mice for each group, one-way ANOVA test). (**G**) Consecutive sections from GSC23 xenografts were subjected to RNAscope and immunohistochemistry (IHC). Representative images are shown. (**H**) Cells were intracranially injected into nude mice as described in (F). The survival of mice was evaluated ($n = 8$ mice, Kaplan-Meier with two-sided log-rank test). Data in (A), (B), and (D) are means ± SEM of three independent experiments.

Human USP16 is an 823–amino acid protein with an ubiquitin protease–like zinc finger domain (UBP-ZnF) in the N terminus and an USP domain in the C terminus (Fig. 5E, left). To identify the domain that mediates USP16's interaction with lncEPAT, we constructed Flag-tagged truncation mutants of USP16 (Fig. 5E, right upper panel). Using those mutants, we found that the UBP-ZnF domain is essential for lncEPAT binding (Fig. 5E, right lower panel), which is consistent with previous findings that the ZnF domain binds to RNAs (*26*, *27*). Moreover, RNA pull-down assays using several truncation mutants of lncEPAT indicated that the 3′-end from 982 to 1399 was required for the binding of lncEPAT to USP16 (Fig. 5F). These results demonstrate that lncEPAT specifically interacts with USP16 in GBM cells.

It has been reported that the UBP-ZnF domain binds to the C terminus of ubiquitin in protein substrates and regulates the

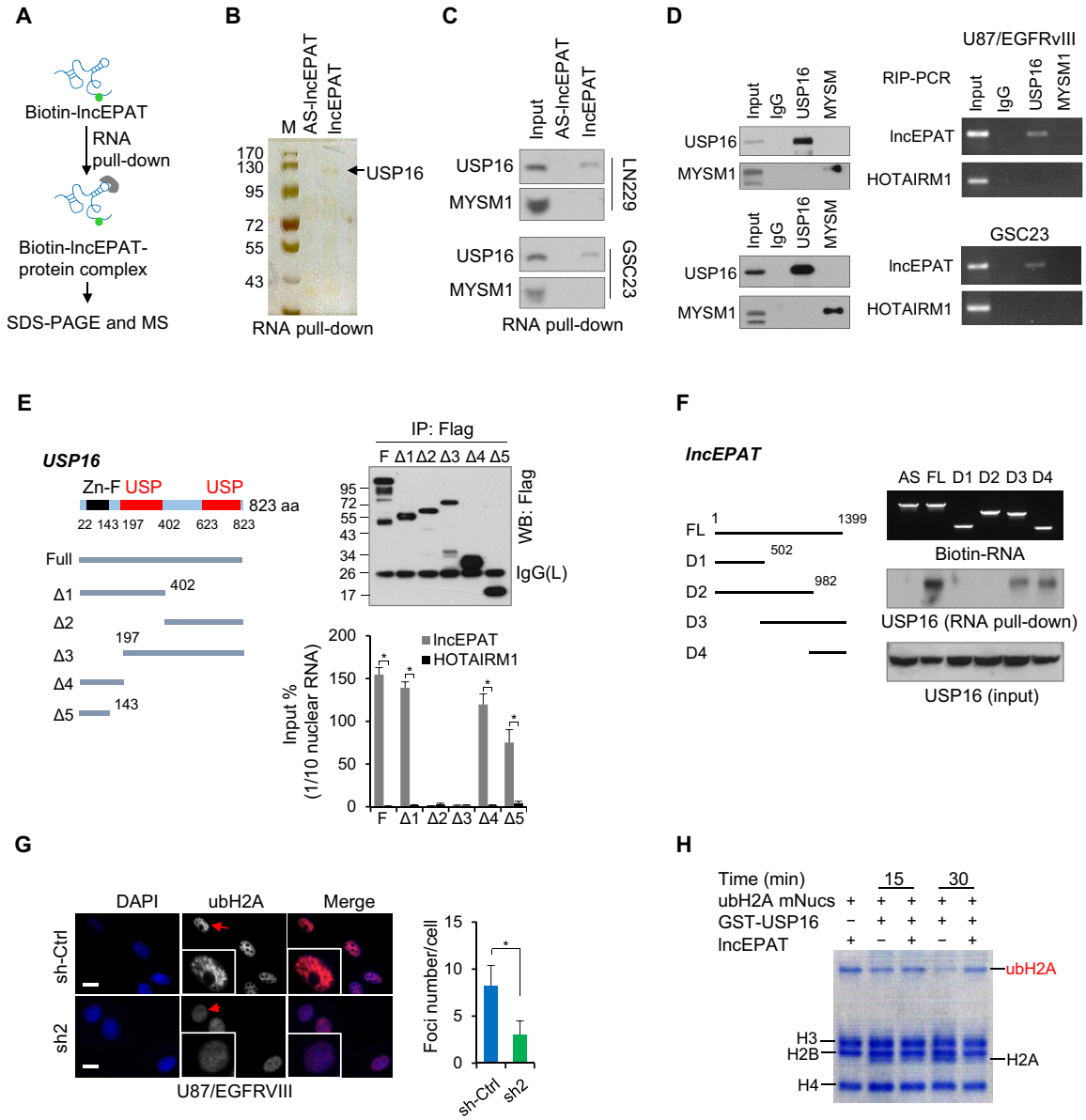

Fig. 5. lncEPAT interacts with USP16 to compromise its deubiquitinase activity. (**A**) Scheme shows the experimental procedure to identify lncEPAT-interacting proteins. (**B**) Biotinylated lncEPAT or AS-lncEPAT incubated with GSC23 nuclear extracts. The RNA-protein complexes were purified with streptavidin-agarose beads and resolved on SDS-PAGE electrophoresis. The specific protein bands, identified by silver staining, were subjected to MS analysis. The arrow indicates the USP16 band. (**C**) Biotinylated lncEPAT or AS-lncEPAT was incubated with GSC23 or LN229 nuclear extracts and then incubated with streptavidin magnetic beads. The purified proteins were subjected to Western blotting. (**D**) RIP assays were performed in U87/EGFRvIII and GSC23 cells using USP16 antibody. The immunoprecipitated RNA was reverse-transcribed and then analyzed by semiquantitative RT-PCR. MYSM1 was used as a control. (**E**) USP16 truncation mutants were transfected into U87/EGFRvIII cells. RIP assays were performed using Flag-tag antibody. The immunoprecipitated RNA was analyzed by qRT-PCR. HOTAIRM1 was used as a control. Values are the percentage to input (means ± SEM of $n = 3$ independent experiments; $^*P < 0.001$, two-tailed Student's t test). (**F**) Biotinylated RNAs of the full-length lncEPAT, AS-lncEPAT, and lncEPAT with deletions were incubated with GSC23 nuclear extracts. The purified proteins were subjected to Western blotting. (**G**) U87/EGFRvIII shRNA cells were analyzed with H2AK119ub1 antibody. Representative images show ubH2A foci. The number of ubH2A foci in each cell was quantified (means ± SD, $n = 6$ randomly selected fields, two-tailed Student's t test). (**H**) Deubiquitinase assay of recombinant mononucleosomes (K119 ubiquitinated histone H2A, ubH2A mNucs) by USP16 with or without lncEPAT.

catalytic activity of deubiquitinases (*28*, *29*). Moreover, USP16 is a primary enzyme that antagonizes H2AK119ub1 (*13*, *14*). USP16 overexpression in GSC2 and GSC23 cells suppressed H2A ubiquitination (fig. S3A). USP16 depletion in GBM and GSC cells increased ubH2A levels (fig. S3B). These results suggest that USP16 is a functional H2A deubiquitinase in glioma cells. We thus determined the effect of lncEPAT on USP16-mediated H2A deubiquitination. Depletion of lncEPAT had no effect on USP16 expression but decreased the level of ubH2A (fig. S3C), whereas overexpression of lncEPAT increased the ubH2A level (fig. S3, D and E). LncEPAT depletion also attenuated ubH2A foci formation in GBM cells (Fig. 5G and fig. S3F). Further, we found that lncEPAT depletion on the levels of ubH2A was reversed

by further depletion of USP16 (fig. S3G). These studies established a link between lncEPAT expression and H2A monoubiquitination levels through USP16.

To explore whether lncEPAT-USP16 interaction inhibits USP16's deubiquitination activity, we carried out a cell-free deubiquitinase assay to test USP16's deubiquitination ability on targeting ubH2A mononucleosomes. Compared with USP16 incubation alone, lncEPAT-USP16 interaction showed higher ubH2A levels and lower H2A levels, which illustrated that this interaction compromised USP16's deubiquitination activity in vitro (Fig. 5H). Together, these data indicated that lncEPAT maintains H2A ubiquitination status by blocking USP16-induced H2A deubiquitination.

EGFR-lncEPAT axis suppresses cell cycle arrest and cell senescence by antagonizing USP16 in GBM cells

To further explore the mechanism of lncEPAT on GBM cell growth, we analyzed the changes in gene expression after lncEPAT depletion in GSC23 cells using microarray assays. A gene set enrichment analysis (GSEA) was used to identify differentially enriched pathways and revealed a signature of gene expression changes related to cell cycle progression and DNA replication (Fig. 6A and table S3). These results are consistent with previous findings that USP16 regulates cell cycle progression and senescence (*9*, *16*). We next detected the expression of the most substantially changed genes that were closely associated with cell senescence, including *CDKN1A* (*30*), *CLUSTERIN* (*31*), and *DKK1* (*32*), and confirmed that they were up-regulated by lncEPAT depletion (Fig. 6B). Moreover, ChIP-seq tracks of binding patterns at individual genes showed that lncEPAT depletion reduced the enrichment of PRC1 (determined by Ring1B antibody) at these senescence-associated gene promoter regions and thereby decreased the ubH2A levels at these gene promoter regions (fig. S4A). In contrast, these effects of lncEPAT depletion were reversed by further depletion of USP16 (fig. S4A). Furthermore, we corroborated this pattern of lncEPAT-dependent USP16/ubH2A occupancy change at the senescence-associated gene promoter regions by ChIP-qPCR (Fig. 6C).

We next evaluated the effect of lncEPAT on cell cycle progression. LncEPAT depletion resulted in an enrichment of cells arrested in the G_1 stage, in U87/EGFRvIII and GSC23 cells (Fig. 6D). However, lncEPAT depletion did not induce apoptosis as judged by the absence of sub-G_1 cells (Fig. 6D). To determine the role of lncEPAT in cell senescence, we detected the senescence-associated β-galactosidase (SA-β-gal) activity of GBM cells and found that lncEPAT depletion increased the percentage of SA-β-gal–positive cells, whereas reconstituted expression of lncEPAT reversed this effect (fig. S4B). These results were further confirmed in GSCs (fig. S4C). Moreover, overexpression of USP16 promoted senescence in GBM cells and GSCs (fig. S4D), while depletion of USP16 reversed the effect of lncEPAT knockdown on GSC senescence (Fig. 6E).

Furthermore, we evaluated the effect of EGFR-lncEPAT axis on cell senescence. We first determined the role of EGF in cell senescence by culturing GSC cells with or without EGF. GSC cells cultured without EGF had higher rate of cell senescence as compared to the cells cultured with EGF, whereas lncEPAT depletion largely reversed the effect of EGF (fig. S4E). In addition, EGF inhibited the expression of these senescence-associated genes, whereas lncEPAT depletion largely reversed the effect of EGF (fig. S4F). Next, we treated cells with gefitinib and found that inhibition of the EGFR pathway promoted cell senescence, whereas lncEPAT overexpression partially reversed the effect of gefitinib (fig. S4G). Together, the above results indicate that the EGFR pathway plays a role in suppression of cell senescence, and that EGFR-induced lncEPAT down-regulates the expression of pro-senescence genes and cell senescence by blocking USP16-mediated H2A deubiquitination.

LncEPAT attenuates USP16-mediated tumor suppression

Although USP16 has been shown to reduce the expansion of normal fibroblasts and neurosphere formation of neural progenitor cells (*16*), its role in tumorigenesis of glioma is unknown. We overexpressed USP16 in GSC23 and GSC2 cells and found that tumor sphere formation and cell proliferation were greatly repressed (Fig. 7, A and B, and fig. S5A). These results were further confirmed by the fact that depleting USP16 promoted cell proliferation in Hs683 and SW1783 cells (fig. S5B).

We next examined the expression of USP16 in different cells, including NHAs, cell lines derived from lower-grade glioma and GBM, and GBM patient-derived GSCs; however, we found no difference in USP16 expression among these cells (Fig. 7C). Moreover, no significant difference in USP16 protein levels was observed between low-grade glioma and GBM tissues (fig. S5C). In contrast, levels of ubH2A were up-regulated in GBM cell lines, especially in GSCs, as compared with lower-grade glioma cell lines and NHAs (fig. S5D). Also, lncEPAT expression positively correlated with glioma grade in cell lines and in human tissues (Fig. 2, A, C, and D). On the basis of these observations, we hypothesized that loss of tumor suppression function of USP16 in GBM cells is likely due to increased lncEPAT expression, although USP16 expression was not decreased in GBMs cells. We found that, in GSC23 and GSC2 cells, depleting USP16 reversed the effect of lncEPAT knockdown on tumor sphere formation and cell proliferation (Fig. 7, D to F). To further investigate the role of USP16 in lncEPAT-induced tumor cell growth, we overexpressed lncEPAT and then USP16 in U87 cells that have low-level lncEPAT. Overexpression of lncEPAT inhibited cell senescence in U87 cells, whereas overexpression of USP16 partially reversed this phenotype induced by lncEPAT overexpression (fig. S5, E and F). Moreover, we found that lncEPAT and USP16 could regulate the same cell senescence–associated genes, but in an opposite way. Overexpression of lncEPAT inhibited the expression of these genes in U87 cells, while overexpression of USP16 in the lncEPAT-overexpressing cells increased the expression of these genes as compared with lncEPAT overexpression alone (fig. S5G). In contrast, depleting lncEPAT promoted the expression of these genes in GSC23 cells, while depleting USP16 partially reversed the effect of lncEPAT depletion on the promotion of these genes (fig. S5, H and I). These results suggest that the function of lncEPAT in tumor cell growth depends, in large part, on antagonizing USP16.

We next explored the role of blockade of USP16 by lncEPAT in gliomagenesis using an in vivo mouse model. Overexpression of lncEPAT in U87 cells increased tumor growth, whereas overexpression of USP16 partially inhibited the tumor growth induced by lncEPAT overexpression (fig. S5J). Also, USP16 overexpression inhibited the tumor formation ability of GSC23 and GSC2 cells (fig. S5K). In xenograft tumor tissues, overexpression of USP16 resulted in an increased number of senescence cells (fig. S5L). These results are consistent with the above in vitro results. Moreover, as we demonstrated previously, depleting lncEPAT attenuated the tumor formation of GSC23 and GSC2 cells and thus improved the overall

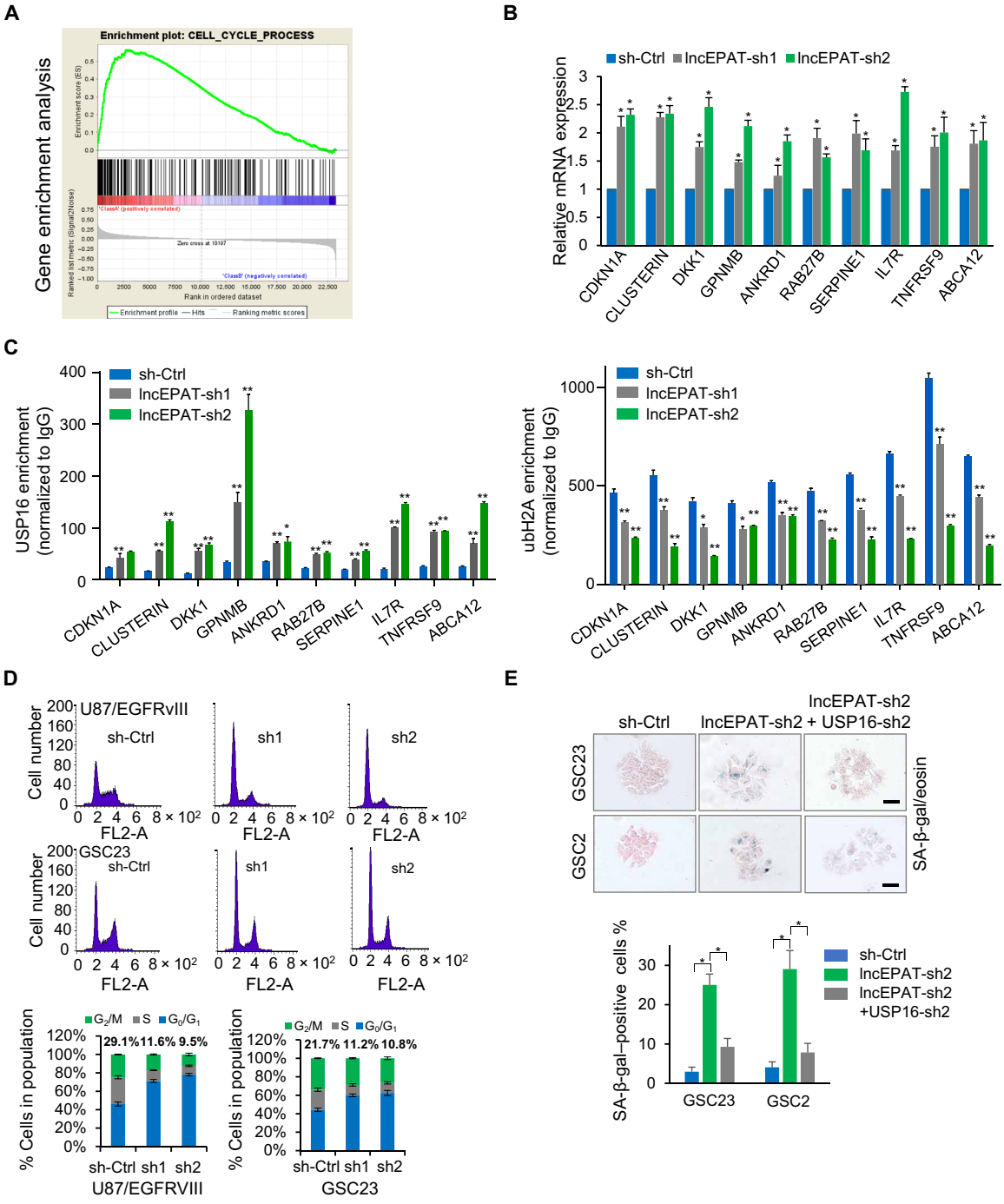

Fig. 6. Depletion of lncEPAT induces GBM cell senescence through USP16. (**A**) Gene enrichment analysis of GSC23 cells shows extensive changes in cell cycle–related genes after depletion of lncEPAT using two independent shRNAs. (**B**) qPCR assays confirmed the most substantially changed genes that were closely related to senescence. GAPDH was used as internal control. Data are means ± SEM of $n = 3$ independent experiments; $^*P < 0.05$, two-tailed Student's t test. (**C**) ChIP-qPCR analysis of USP16 enrichment and ubH2A enrichment at senescence-associated gene promoter region upon lncEPAT knockdown. ChIP-qPCR was performed in GSC23 (sh-Ctrl) and GSC23 (lncEPAT-sh1 and lncEPAT-sh2) cell lines. Data are means ± SEM of $n = 3$ independent experiments. $^*P < 0.05$ and $^{**}P < 0.01$, multiple t test. (**D**) U87/EGFRvIII and GSC23 cells expressing lncEPAT shRNAs were analyzed by flow cytometry. Representative images are shown (left panel). Percentages of cells in the population were quantified (right panel). Data are means ± SEM of $n = 3$ independent experiments. (**E**) GSC23 and GSC2 cells expressing lncEPAT shRNA or lncEPAT shRNA plus USP16 shRNA were stained to determine SA-β-gal activity. Representative images are shown (upper panel). Scale bar, 100 μm. Percentages of SA-β-gal–positive cells were counted (lower panel; means ± SD of $n = 6$ randomly selected microscope fields; $^*P < 0.05$, two-tailed Student's t test).

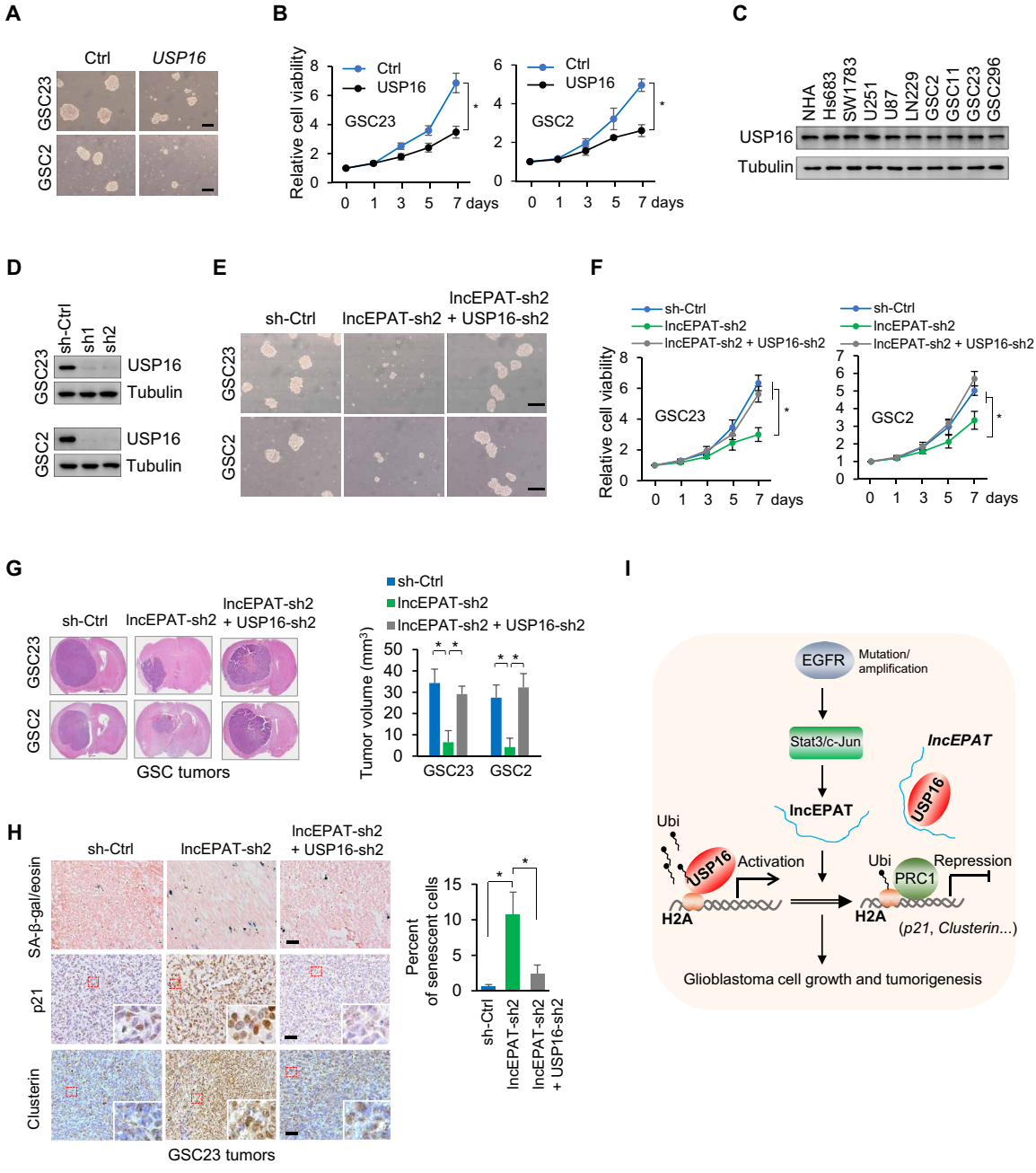

Fig. 7. The role of blockade of USP16 by lncEPAT in regulating senescence-like cell growth suppression and GBM tumorigenesis. (**A**) GSC23 and GSC2 cells stably expressing USP16 were analyzed using neurosphere formation assays. Scale bar, 200 μm. (**B**) The proliferation of GSC23 and GSC2 cells expressing USP16 was analyzed by XTT assays. Relative cell viabilities were normalized to those at day 0 (means ± SEM of $n = 3$ independent experiments; *$P < 0.01$, two-tailed Student's t test). (**C**) The cell lysates from different cells were analyzed by Western blot analysis using anti-USP16 antibody. (**D**) Stable GSC23 and GSC2 cells expressing two independent USP16 shRNAs were analyzed by Western blot analysis. (**E** and **F**) Stable GSC23 and GSC2 cells expressing lncEPAT shRNA2 or lncEPAT shRNA2 plus USP16 shRNA2 were analyzed using neurosphere formation assays (E) and cell viability assays (F). Scale bar, 200 μm. Data are means ± SEM of $n = 3$ independent experiments; *$P < 0.01$, two-tailed Student's t test. (**G**) Stable GSC23 and GSC2 cells (5×10^5 cells per mouse) expressing lncEPAT shRNA2 or lncEPAT shRNA2 plus USP16 shRNA2 were intracranially injected into nude mice. Tumor volumes were calculated (right panel; means ± SD of $n = 8$ mice for each group; *$P < 0.01$, one-way ANOVA test). (**H**) GSC23 tumor tissues were stained by SA-β-gal/eosin, p21, and Clusterin. Scale bar, 100 μm. The percentage of senescent cells was quantified (means ± SD of $n = 6$ random selected microscope fields; *$P < 0.05$, two-tailed Student's t test). (**I**) Diagram showing the EGFR-lncEPAT-USP16 regulatory cascades in gliomagenesis.

survival of the mice bearing the tumor cells, but these effects were partially reversed by further depletion of USP16 (Fig. 7G and fig. S5M). The number of senescence cells was significantly increased in xenograft tumor tissues with lncEPAT depletion than in controls, whereas depleting USP16 reversed this effect of lncEPAT depletion (Fig. 7H). Accordingly, the expression of p21 and Clusterin as senescence markers was induced by the depletion of lncEPAT but reversed by depletion of USP16 (Fig. 7H). These results consistently support the critical role that the antagonizing of USP16 by lncEPAT plays in cell proliferation and glioma tumorigenesis by inducing tumor cell senescence. Together, the above data indicated that lncEPAT interacts with USP16 and inhibits USP16-mediated H2A deubiquitination and senescence-associated gene expression, hence blocking USP16's role on tumor suppression.

DISCUSSION

Dysregulated EGFR signaling is a critical driver of GBM development and therapy resistance. In the current study, we characterized a previously unidentified oncogenic lncRNA, lncEPAT, which was induced by EGFR signaling activation. We demonstrated that lncEPAT interacts with USP16 to inhibit H2A deubiquitination and repress target gene expression. The lncEPAT level is positively correlated with the glioma grade and predictive of survival in glioma patients. Moreover, lncEPAT is required for GBM cell proliferation and tumorigenesis by suppressing USP16-triggered senescence program (Fig. 7I). Thus, our data consistently support that EGFR-lncEPAT-ubH2A coupling represents a critical mechanism controlling epigenetic gene regulation and senescence resistance in GBM tumorigenesis.

Ubiquitination of histone H2A plays a critical role in remodeling chromatin and mediates the epigenetic regulation of gene transcription. This modification can be present in up to 10% of total H2A in chromatin as a result of the ubiquitination of H2A Lys^{119} (*9*, *33*). H2AK119 ubiquitination is primarily catalyzed by the PRC1 complex and has been linked to gene repression. Ring1B, as a part of the PRC1, acts as a major E3 ubiquitin ligase of histone H2A monoubiquitination, whereas Bim1 is the scaffold for assembling the ubiquitin ligase complex (*34*). In addition, during cellular response to DNA damage, RNF8/RNF168 catalyzes H2A ubiquitination at $Lys^{13/15}$, which is required for the efficient recruitment of downstream repair proteins, such as 53BP1, to promote the DNA damage checkpoint and resistance to ionizing radiation (*33*, *35*). Because USP16 also deubiquitinates ubH2A Lys^{15} (*36*), lncEPAT may be involved in the regulation of DNA damage response by blocking the USP16-mediated deubiquitination of ubH2A-K15; this will be an interesting subject for future study.

USP16 overexpression contributes to reduced expansion of normal fibroblasts and the neurosphere formation of neural progenitor cells, which are caused by the up-regulation of antiproliferative genes, including *p16* and *p21* (*16*). The antiproliferative effect of USP16 was confirmed in our study using glioma cells and patient-derived GSCs. However, USP16 is ubiquitously expressed in normal astrocytes and glioma cells, with no notable difference between low-grade glioma and GBM. This apparent controversy can be explained by the critical role of lncEPAT, which acts as a node to regulate USP16's interaction with and deubiquitination of H2A. Because the lncEPAT level is up-regulated in GBM and correlated with glioma grade, lncEPAT may act as a specific regulator that controls USP16-mediated H2A deubiquitination and gene expression during tumorigenesis. Although in this study we have demonstrated that USP16 has an antitumor growth function in glioma, please note that USP16's role in cancers might be tumor type specific. A previous report shows that USP16 down-regulation promoted Hepatocellular carcinoma (HCC) tumorigenicity and malignancy (*37*). In contrast, down-regulation of USP16 markedly suppressed prostate cancer cell growth both in vitro and in vivo (*38*). Also, USP16 plays an oncogenic role in K-RAS–driven lung tumorigenesis (*39*). The functions of USP16 in different tumors seem dependent on different downstream targets of USP16. Nevertheless, the results of our work for the USP16's function in glioma and glioma stem cells are consistent with the previous results that USP16 overexpression impaired cell proliferation in neural progenitors, and that USP16 regulated senescence in stem cells and progenitor cells of multiple tissues (*16*).

Cellular senescence is a state of permanent cell cycle arrest and loss of proliferative potential and has often been considered to be functionally similar to apoptosis as an intrinsic tumor suppressor mechanism (*40*). The process of neoplastic transformation involves a series of cellular events that allow cells to bypass senescence. Tumor cells have retained the capacity to senesce. Most conventional anticancer therapies, such as chemotherapy, activate DNA damage signaling, which induces senescence-like cell growth arrest rather than apoptotic cell death (*41*). Pro-senescence therapy has been suggested as a promising strategy for cancer treatment (*40*, *42*). Reactivation of p53 in tumors has been shown to elicit robust tumor regression, mediated by senescence induction (*43*, *44*), and compounds that enhance p53 activity are currently in phase 2 clinical trials to treat cancer (NCT02965950). In this study, we revealed that lncEPAT interrupts USP16-mediated H2A deubiquitination of target genes, leading to up-regulation of genes associated with cell senescence to trigger the senescence program. Upon lncEPAT depletion, we found that many genes involved in cell senescence were up-regulated, including *CDKN1A* and *CLUSTERIN*. Thus, targeting lncEPAT may represent a pro-senescence therapeutic strategy that reactivates cell senescence program to control the growth of GBM cells. At present, little is known regarding lncEPAT's downstream targets and molecular mechanisms. In the current study, we present compelling evidence that lncEPAT's function in GBM is at least in part dependent on USP16 inactivation. However, we anticipate that lncEPAT has multiple downstream targets and that lncEPAT may affect tumor growth via multiple mechanisms. Studying the USP16-independent mechanism would provide an improved understanding of lncEPAT in GBM. Therefore, we will actively explore this important aspect in the near future.

EGFR signaling is closely involved in the regulation of cellular senescence process. Fibroblasts approaching senescence present decreased expression of EGFR (*45*). Further, inhibition of EGFR arrests mammalian cell growth by inducing cellular senescence (*7*). In cancer, inhibiting EGFR sensitizes NSCLC cells to radiotherapy by activating the senescence program (*8*). Moreover, down-regulation of EGFR signaling by pharmacologic inhibition or RNA interference induces human GBM senescence and inhibits growth of tumor xenografts (*46*). These studies indicate an anti-senescence role of EGFR signaling facilitating tumorigenesis. Our study revealed an EGFR-lncEPAT-USP16 regulatory axis, which integrates EGFR dysregulation with H2A ubiquitination to repress cellular senescence and promote tumor formation. The identification of EGFR-induced, GBM-overexpressed lncEPAT provides a new target for pro-senescence therapy in GBM.

MATERIALS AND METHODS

Cell culture and treatment

293T, 293FT, NHA, SW1783, Hs683, LN229, LN229/EGFRvIII-Tet-On, U251, U87, U87/EGFR-wt, and U87/EGFRvIII cells were cultured in Dulbecco's modified Eagle's medium (DMEM) supplemented with 10% bovine calf serum (HyClone). Patient-derived GSCs (GSC2, GSC11, GSC23, and GSC262) were maintained in DMEM/F-12 (50:50) medium supplemented with B27, EGF (10 ng/ml), and basic fibroblast growth factor (FGF; 10 ng/ml), as we described previously (*47*). Only early-passage GSC cells were used in the study. No cell lines used in this study were found in the database of commonly misidentified cell lines that is maintained by International Cell Line Authentication Committee (ICLAC) and National Center for Biotechnology Information (NCBI) Biosample. Cell lines were authenticated by short tandem repeat profiling and routinely tested for mycoplasma contamination.

U87/EGFR-wt cells were serum-starved overnight and then treated with EGF (50 ng/ml; Life Technologies, Carlsbad, CA) for different time intervals. GSC23 cells were cultured in DMEM/F-12 medium deprived of EGF and FGF for 24 hours and then treated with EGF (50 ng/ml) for different time intervals. LN229/EGFRvIII Tet-On cells were treated with different concentrations of doxycycline to induce the overexpression of EGFRvIII.

Human tissue samples

Anonymous archived human GBM specimens were obtained from The University of Texas MD Anderson Cancer Center. All tissue samples were collected in compliance with the institution's informed consent policy. The use of the tissue samples was approved by the Institutional Review Boards of the University of Texas MD Anderson Cancer Center.

Antibodies and small interfering RNAs

Detailed information about all antibodies used in this study is shown in table S4. All small interfering RNAs (siRNAs) were synthesized from Sigma-Aldrich, and the target sequences of the siRNAs are shown in table S5.

Plasmids

Full-length lncEPAT was amplified by RT-PCR from the U87/EGFRvIII cDNA library and cloned into pLVX-puro plasmid to form the pLVX-puro-lncEPAT plasmid. LncEPAT deletion mutants D1 to D4 (1 to 502 nt, 1 to 982 nt, 502 to 1399 nt, and 982 to 1399 nt) were amplified by PCR from the full-length pLVX-puro-lncEPAT plasmid and then cloned into pLVX-puro plasmid to form the lncEPAT deletion mutant plasmids. USP16 truncation fragments (corresponding to 1 to 402, 402 to 823, 197 to 823, 1 to 197, and 1 to 143 amino acids) were amplified by PCR from the full-length Flag-USP16 plasmid and cloned into pcDNA3.1-Flag plasmid to generate USP16 truncation mutant plasmids. Full-length cDNA of human USP16 was also amplified by PCR from the full-length Flag-USP16 plasmid and subcloned into pLVX-puro/pLVX-neo and pGEX-4T-1 to generate pLVX-puro-USP16/pLVX-neo-USP16 and pGEX-4T-1-USP16 plasmids. Primers used for PCR are shown in table S5.

LncEPAT shRNA expression plasmids were constructed by annealing the sense and antisense oligonucleotides of the target sequence and cloned into pLKO.1-neo vector. LncEPAT promoter was amplified from U87/EGFRvIII genome DNA by PCR and cloned into pGL3-basic vector. USP16 shRNA plasmids were obtained from Sigma-Aldrich (sh1, TRCN0000434649; sh2, TRCN0000436256). All plasmids were verified by DNA sequencing. Oligonucleotides for the construction of shRNA expression plasmids are shown in table S5.

Lentiviral transduction and selection

Lentiviral vectors and ViraPower lentiviral packaging mix (Life Technologies) were transfected into 293FT cells using X-tremeGENE HP transfection reagent (Roche). Culture medium was changed 8 hours after transfection, and lentivirus was collected 24 hours later. Glioma cells or GSCs in six-well plates were infected by lentivirus and then selected by puromycin (2 μg/ml) or neomycin (200 μg/ml) for 1 week.

Analysis of GEO dataset

The microarray data were extracted from the Gene Expression Omnibus (GEO) public database at NCBI (GSE4290), in which 23 samples from epilepsy patients were used as nontumor samples and 157 tumor samples of different grade were included. The CEL files were normalized to a median intensity array, and model-based expression values were normalized using MAS5 in Bioconductor. The resulting matrix was used as an input for fold change (FC) analysis, and differentially expressed genes between different comparison groups (FC > 1.5) were used for the Venn diagram visualization.

RNA FISH analysis

Stellaris FISH probes (CAL Fluor Red 590 dye) were designed and synthesized by Biosearch Technologies. An RNA FISH analysis was performed according to the manufacturer's instructions (Biosearch Technologies). In brief, GBM cells with the indicated treatment were fixed by 3.7% formaldehyde in phosphate-buffered saline (PBS) at ambient temperature for 10 min. Cells were permeabilized by 70% ethanol for at least 2 hours at 2° to 8°C and then incubated with 100 nM FISH probes in hybridization buffer [dextran sulfate (100 mg/ml) and 10% formamide in 2× SSC] at 37°C overnight. Slides were washed and incubated with 4′,6-diamidino-2-phenylindole (DAPI; 5 ng/ml) for 15 min. Images were taken using a deconvolution microscope (Zeiss) with a 63-Å oil immersion objective. AxioVision software from Zeiss was used to deconvolve Z-series images.

Immunofluorescence and immunohistochemical analysis

Immunofluorescence was performed as we described previously (*48*). U87/EGFRvIII or GSC23 cells in six-well plates were treated with 4% formaldehyde for 5 min and then treated with 0.5% Triton X-100 for 5 min. The slides were incubated with an antibody against H2AK119ub1 (Cell Signaling Technology; 1:500) and then incubated with a fluorescent-conjugated secondary antibody (Alexa Fluor 594, Life Technologies; 1:1000). Nuclei were costained with DAPI. Images were taken using a deconvolution microscope (Zeiss).

For immunohistochemical staining, tissue slides were deparaffinized, rehydrated through an alcohol series, and then stained with primary antibodies against USP16, p-EGFR (Y1068), p21, Clusterin, Ki-67, and PCNA (see table S4 for detailed information about the concentration of each antibody). We quantified the score of USP16 and p-EGFR staining according to the percentage of cells with positive staining and the staining intensity, as we performed previously (*48*). Briefly, staining was scored according to the percentage of cells with positive staining and the staining intensity. We assigned the

percentage score as follows: 0 if no cell had staining, 1 if 0 to 25% of cells had staining, 2 if 25 to 50% of cells had staining, 3 if 50 to 75% of cells had staining, and 4 if more than 75% of cells had staining. We scored the staining intensity as 0 for negative, 1 for weak, 2 for moderate, and 3 for strong. The total score was obtained by multiplying the percentage score by the intensity score. Three individuals who were blinded to the slides examined and scored each sample. The final score was the median value of the scores provided by the individuals.

RNAscope

In situ detection of lncEPAT in human glioma specimens was performed using probes synthesized by Advanced Cell Diagnostics and an RNAscope 2.0 detection kit (BROWN, Advanced Cell Diagnostics), according to the manufacturer's instructions. Thirty-four anonymous archived human GBM specimens were obtained from MD Anderson under a protocol approved by the institutional review board. The brain cancer tissue microarray was obtained from Biomax (BS17017a, containing 32 cases of astrocytoma, 27 GBM, and 4 adjacent normal brain tissue).

The NSCLC tissue microarray was also obtained from Biomax (LC1006, containing 45 cases of paired NSCLC and tumor-adjacent normal tissue and 9 cases of normal lung tissue from autopsy and two unmatched tumor-adjacent normal tissues). We quantitatively scored lncRNA expression on the tissue sections according to the percentage of positive cells and the staining intensity, as described in immunohistochemical analysis. The total score was obtained by multiplying the percentage score by the intensity score. Three individuals who were blinded to the slides examined and scored each sample. The final score was the median value of the scores provided by the individuals.

RNA extraction and RT-PCR

Total RNA was extracted using TRIzol reagent (Invitrogen) and reverse-transcribed using iScript Reverse Transcription Supermix (Bio-Rad), according to the manufacturer's instructions. The reverse-transcribed cDNA products were used for qPCR analysis with SYBR Select Master Mix (Life Technologies). Primers for the lncRNA real-time PCR analysis were obtained from Sigma-Aldrich. Glyceraldehyde-3-phosphate dehydrogenase (GAPDH) was used as an internal control. The sequences of all other quantitative RT-PCR primers are shown in table S5. All data are given as means ± SEM of three independent samples.

5′ RACE

Rapid amplification of lncEPAT 5′ cDNA end was performed using the 5′ RACE Kit (Life Technologies) according to the manufacturer's instructions. The resulting PCR product was cloned into the T-Vector and then sequenced. Primers for 5′ RACE are shown in table S5.

RNA immunoprecipitation

RIP was performed using a Magna RIP RNA binding protein immunoprecipitation kit (17-770, Merck Millipore), according to the manufacturer's instructions. In brief, 1×10^7 U87/EGFRvIII or GSC23 cells were collected and rinsed with PBS. After cell lysis, the nuclear membranes and debris were pelleted by centrifugation at 15,000*g* for 15 min at 4°C. The magnetic bead–antibody complex was prepared by adding 5 μg of USP16 antibody (Santa Cruz Biotechnology) or control immunoglobulin G (Cell Signaling Technology) into magnetic beads (50 μl per sample) in RIP wash buffer. The cell lysates were then incubated with magnetic bead–antibody complex overnight at 4°C. The bead-antibody-RNA complex was washed with RIP wash buffer three times, and RNA was purified. The immunoprecipitated RNA was analyzed by quantitative RT-PCR using gene-specific primers (table S5).

Microarray analysis of gene expression

We analyzed the differences in gene transcription after knocking down lncEPAT in the Sequencing and Microarray Facility at MD Anderson using the Affymetrix GeneChip Human Gene 1.0 ST array (Affymetrix). The genes showing altered expression (FC > 1.5) compared with the control shRNA were selected and analyzed using GSEA.

RNA in vitro transcription, RNA pull-down, and MS

RNA in vitro transcription was performed using a MEGAscript T7 transcription kit (Life Technologies), according to the manufacturer's instructions. DNA templates were amplified by PCR from pLVX-puro-lncEPAT plasmid using the primers shown in table S5. F1/R1, F1/R2, F1/R3, F2/R1, or F3/R1 DNA template (1 μg) was incubated with adenosine triphosphate (ATP), cytidine triphosphate (CTP), guanosine triphosphate (GTP), and uridine triphosphate (UTP)/biotin-16-UTP (UTP:biotin-16-UTP = 2:1) in the presence of RNA transcription enzyme mix. The transcribed RNAs were purified by lithium chloride solution and 70% ethanol.

To identify the proteins associated with lncEPAT, we incubated in vitro–transcribed biotin-lncEPAT with nuclear lysates of GSC23 cells and then with Dynabeads MyOne Streptavidin C1 (Life Technologies). The isolated proteins were separated by SDS-PAGE, followed by sliver staining (Thermo Fisher Scientific). Protein bands of interest were excised and subjected to MS analysis (UT Health Clinical and Translational Proteomics Service Center). MS/MS spectra were searched against the UniProt Homo Sapiens Reference Proteome dataset using Mascot v2.5.1 (Matrix Science).

SA-β-gal staining

SA-β-gal staining was performed using the senescence detection kit (QIA117-1 kit, Millipore), according to the manufacturer's instructions. Cryosections or cultured cells were incubated with staining solution for 16 hours at 37°C. Sections were counterstained with eosin and mounted using 70% glycerin. Images were taken under a bright-field microscope.

Northern blot

Northern blot was performed using the DIG Northern Starter Kit (Roche, Germany), according to the manufacturer's instruction. Briefly, lncEPAT DNA was amplified by PCR, and RNA was labeled in an in vitro transcription reaction with digoxigenin-11-UTP using the T7 RNA Polymerase. Total RNA from U87 or U87/EGFRvIII cells (15 μg) was separated by gel electrophoresis with a 1% denaturing formaldehyde gel in 1× Mops buffer and transferred onto nylon membrane. The membrane was incubated with the Dig-labeled lncEPAT probe and then with the antibody solution. The signals were detected by exposing the membrane to an x-ray film. Primers used for PCR amplification are shown in table S5.

Promoter reporter gene assay

LncEPAT full-length promoter reporter pGL3-wt was constructed by cloning the fragment (−3000/+1) upstream of lncEPAT TSS into

pGL3-Basic vector, and the sequence of the promoter was confirmed by DNA sequencing. Next, we generated mutated promoter reporters containing c-Jun or Stat3 binding site mutations using a QuikChange II site-directed mutagenesis kit (Agilent Technologies). Specially, the mutations were made by changing base pairs of pGL3-wt as the following: c-Jun binding site 1 from TGAGTCA to TGGGTCG (pGL3-mutS1), c-Jun binding site 2 from TCACTCA to TCGCTCG (pGL3-mutS2), and Stat3 binding sites 3 and 4 from TTCTTAGAATTTAGGGAA to TGCTTAGCATTGAGGGCA (pGL3-mutS3 + S4).

The pGL3 reporter plasmids and internal control plasmid pRL-TK were transfected into LN229/EGFRvIII Tet-on cells. Thirty-six hours after transfection, cells were lysed and reporter gene expression was analyzed using a Dual-Luciferase Reporter assay system (Promega).

ChIP-qPCR

ChIP assays were performed as described previously (*49*). Briefly, GBM cells were cross-linked with 1% formaldehyde for 10 min at room temperature and quenched with 125 mM glycine. The isolated nuclei were resuspended in nuclei lysis buffer and pulse-sonicated. The samples were immunoprecipitated with 5 μg of indicated antibodies overnight at 4°C and then incubated with protein A/G beads for 1 hour. The immunoprecipitates were washed with low salt, high salt, and LiCl buffers, and the immunoprecipitated DNA was reverse-crosslinked and purified. The resultant DNA was analyzed by semiquantitative RT-PCR and determined by electrophoresis in a 2% agarose gel or by real-time qPCR on the ABI 7500-FAST System using the SYBR Green PCR Master Mix (Applied Biosystems). Primers used for qRT-PCR are shown in table S5.

For ChIP-seq, ChIP experiments were performed as above using a Ring1B or ubH2AK119 antibody. The ChIP-seq reads were trimmed by Trim Galore (v0.4.4_dev) and mapped to the human genome (hg38 version) using Bowtie (v1.2.2). The resulting sorted BAM files were converted into bedGraph and bigWig formats using BEDTools (v2.24.0) and UCSC bedGraphToBigWig (v4). The ChIP-seq peaks were identified by MACS2 (v2.1.2) with the parameters "macs2 callpeak -t ChIP.bam -c INPUT.bam -g hs --outdir output -n NAME 2> NAME.callpeak.log." BETA (v1.0.7) was used to annotate the peaks that are associated with genes of interest (false discovery rate < 0.05). On the basis of the fold enrichment, differential binding peaks were analyzed among different groups.

Cell growth assays

For the soft agar cell growth analysis, GBM cells (1000 cells per well) were resuspended in DMEM containing 0.3% soft agar and cultured at 37°C in a humidified CO_2 incubator for 10 days. Colonies were stained with 0.05% crystal violet, and those that were >1 mm in diameter were counted. The viability of glioma cells was assessed by XTT assays (Sigma-Aldrich), according to the manufacturer's instructions. Neurosphere formation assays were performed as described previously (*48*).

In vivo GBM mouse model

All mouse experiments were approved by MD Anderson Cancer Center Institutional Animal Care Use for Research Committee (IACUC) and Virginia Commonwealth University IACUC. All animal experiments followed MD Anderson Cancer Center IACUC, Virginia Commonwealth University IACUC, and American Association for Laboratory Animal Science (AALAS) guidelines. The sample sizes were justified by statistical considerations and statistical power analyses. The animals were randomly assigned to different experimental groups. The investigators were blinded to allocation during experiments and outcome assessment. U87/EGFRvIII, GSC23, and GSC2 cells (5×10^5 cells per mouse) expressing the indicated shRNAs or proteins were injected intracranially into 6- to 8-week-old nude (nu/nu) mice, as described previously (*48*). At the end of the experiment, the mice were humanely euthanized, and mouse's brain was harvested, fixed in 4% formaldehyde, and embedded in paraffin. Tumor formation was determined by a histologic analysis of hematoxylin and eosin (H&E)–stained tissue sections. Tumor volumes were calculated using the formula $V = (\pi/6) \times a^2 \times b$, where a and b are the tumor's short axis and long axis, respectively (*48*, *50*). Data are means ± SD of eight or five mice. In a set experiment to analyze mouse survival, animals (8 or 10 mice per group) were humanely euthanized when they were moribund; the remaining animals were humanely euthanized 60 days (U87/EGFRvIII) or 120 days (GSC23) after tumor cell injection.

Deubiquitinase assay

pGEX-GST-USP16 plasmid was transformed into BL21 *Escherichia coli*, and expression was induced by 0.5 mM isopropyl-β-D-thiogalactopyranoside at 16°C overnight. H2AK119 ubiquityl recombinant mononucleosomes (ubH2A mononucleosomes) were bought from EpiCypher. Deubiquitination reactions were performed as described previously (*12*). The reaction was terminated and resolved on SDS-PAGE and stained by Coomassie blue.

Statistical analyses

GraphPad Prism Pro 5.0 software was used for all data analyses. Data are presented as means ± SD or SEM. All Western blot analyses were repeated three times unless otherwise indicated. For all representative images, results were reproduced at least three times in independent experiments. For all quantitative data, the statistical test used is indicated in the figure legends. We assessed differences in the human GBM multiforme data using the Pearson correlation test, the in vitro data between two groups (=2 groups) using the two-tailed Student's t test, the in vitro data among multiple groups (>2 groups), and the in vivo data using two-way analysis of variance (ANOVA). Mouse survival was analyzed using a Kaplan-Meier model. We considered $P < 0.05$ to be significant.

SUPPLEMENTARY MATERIALS

Supplementary material for this article is available at https://science.org/doi/10.1126/sciadv.abn2571

View/request a protocol for this paper from *Bio-protocol*.

REFERENCES AND NOTES

1. G. Reifenberger, H. G. Wirsching, C. B. Knobbe-Thomsen, M. Weller, Advances in the molecular genetics of gliomas—Implications for classification and therapy. *Nat. Rev. Clin. Oncol.* **14**, 434–452 (2017).
2. D. A. Bhowmick, Z. P. Zhuang, S. D. Wait, R. J. Weil, A functional polymorphism in the EGF gene is found with increased frequency in glioblastoma multiforme patients and is associated with more aggressive disease. *Cancer Res.* **64**, 1220–1223 (2004).
3. P. H. Huang, A. M. Xu, F. M. White, Oncogenic EGFR signaling networks in glioma. *Sci. Signal.* **2**, re6 (2009).
4. F. B. Furnari, T. F. Cloughesy, W. K. Cavenee, P. S. Mischel, Heterogeneity of epidermal growth factor receptor signalling networks in glioblastoma. *Nat. Rev. Cancer* **15**, 302–310 (2015).
5. N. Tebbutt, M. W. Pedersen, T. G. Johns, Targeting the ERBB family in cancer: Couples therapy. *Nat. Rev. Cancer* **13**, 663–673 (2013).
6. T. F. Cloughesy, W. K. Cavenee, P. S. Mischel, Glioblastoma: From molecular pathology to targeted treatment. *Annu. Rev. Pathol. Mech. Dis.* **9**, 1–25 (2014).

7. P. B. Alexander, L. F. Yuan, P. Y. Yang, T. Sun, R. Chen, H. D. Xiang, J. K. Chen, H. Y. Wu, D. R. Radiloff, X.-F. Wang, EGF promotes mammalian cell growth by suppressing cellular senescence. *Cell Res.* **25**, 135–138 (2015).
8. M. Wang, F. Morsbach, D. Sander, L. Gheorghiu, A. Nanda, C. Benes, M. Kriegs, M. Krause, E. Dikomey, M. Baumann, J. Dahm-Daphi, J. Settleman, H. Willers, EGF receptor inhibition radiosensitizes NSCLC cells by inducing senescence in cells sustaining DNA double-strand breaks. *Cancer Res.* **71**, 6261–6269 (2011).
9. H. Wang, L. Wang, H. Erdjument-Bromage, M. Vidal, P. Tempst, R. S. Jones, Y. Zhang, Role of histone H2A ubiquitination in polycomb silencing. *Nature* **431**, 873–878 (2004).
10. M. Sauvageau, G. Sauvageau, Polycomb Group Proteins: Multi-faceted regulators of somatic stem cells and cancer. *Cell Stem Cell* **7**, 299–313 (2010).
11. N. P. Blackledge, N. R. Rose, R. J. Klose, Targeting Polycomb systems to regulate gene expression: Modifications to a complex story. *Nat. Rev. Mol. Cell Biol.* **16**, 643–649 (2015).
12. S. Y. Cai, R. W. Babbitt, V. T. Marchesi, A mutant deubiquitinating enzyme (Ubp-M) associates with mitotic chromosomes and blocks cell division. *Proc. Natl. Acad. Sci. U.S.A.* **96**, 2828–2833 (1999).
13. H.-Y. Joo, L. Zhai, C. Yang, S. Nie, H. Erdjument-Bromage, P. Tempst, C. Chang, H. Wang, Regulation of cell cycle progression and gene expression by H2A deubiquitination. *Nature* **449**, 1068–1072 (2007).
14. Y. Gu, A. E. Jones, W. Yang, S. Liu, Q. Dai, Y. Liu, C. S. Swindle, D. Zhou, Z. Zhang, T. M. Ryan, T. M. Townes, C. A. Klug, D. Chen, H. Wang, The histone H2A deubiquitinase Usp16 regulates hematopoiesis and hematopoietic stem cell function. *Proc. Natl. Acad. Sci. U.S.A.* **113**, E51–E60 (2016).
15. W. Yang, Y.-H. Lee, A. E. Jones, J. L. Woolnough, D. Zhou, Q. Dai, Q. Wu, K. E. Giles, T. M. Townes, H. Wang, The histone H2A deubiquitinase Usp16 regulates embryonic stem cell gene expression and lineage commitment. *Nat. Commun.* **5**, 3818 (2014).
16. M. Adorno, S. Sikandar, S. S. Mitra, A. Kuo, B. N. Di Robilant, V. Haro-Acosta, Y. Ouadah, M. Quarta, J. Rodriguez, D. L. Qian, V. M. Reddy, S. Cheshier, C. C. Garner, M. F. Clarke, Usp16 contributes to somatic stem-cell defects in Down's syndrome. *Nature* **501**, 380–384 (2013).
17. J. J. Quinn, H. Y. Chang, Unique features of long non-coding RNA biogenesis and function. *Nat. Rev. Genet.* **17**, 47–62 (2016).
18. J. M. Engreitz, N. Ollikainen, M. Guttman, Long non-coding RNAs: Spatial amplifiers that control nuclear structure and gene expression. *Nat. Rev. Mol. Cell Biol.* **17**, 756–770 (2016).
19. M. Huarte, The emerging role of lncRNAs in cancer. *Nat. Med.* **21**, 1253–1261 (2015).
20. A. M. Schmitt, H. Y. Chang, Long noncoding RNAs in cancer pathways. *Cancer Cell* **29**, 452–463 (2016).
21. W. Pao, J. Chmielecki, Rational, biologically based treatment of EGFR-mutant non-small-cell lung cancer. *Nat. Rev. Cancer* **10**, 760–774 (2010).
22. F. Liu, G. C. Hon, G. R. Villa, K. M. Turner, S. Ikegami, H. J. Yang, Z. Ye, B. Li, S. Kuan, A. Y. Lee, C. Zanca, B. W. Wei, G. Lucey, D. Jenkins, W. Zhang, C. L. Barr, F. B. Furnari, T. F. Cloughesy, W. H. Yong, T. C. Gahman, A. K. Shiau, W. K. Cavenee, B. Ren, P. S. Mischel, EGFR mutation promotes glioblastoma through epigenome and transcription factor network remodeling. *Mol. Cell* **60**, 307–318 (2015).
23. C. W. Brennan, R. G. W. Verhaak, A. McKenna, B. Campos, H. Noushmehr, S. R. Salama, S. Y. Zheng, D. Chakravarty, J. Z. Sanborn, S. H. Berman, R. Beroukhim, B. Bernard, C. J. Wu, G. Genovese, I. Shmulevich, J. Barnholtz-Sloan, L. H. Zou, R. Vegesna, S. A. Shukla, G. Ciriello, W. K. Yung, W. Zhang, C. Sougnez, T. Mikkelsen, K. Aldape, D. D. Bigner, E. G. Van Meir, M. Prados, A. Sloan, K. L. Black, J. Eschbacher, G. Finocchiaro, W. Friedman, D. W. Andrews, A. Guha, M. Iacocca, B. P. O'Neill, G. Foltz, J. Myers, D. J. Weisenberger, R. Penny, R. Kucherlapati, C. M. Perou, D. N. Hayes, R. Gibbs, M. Marra, G. B. Mills, E. Lander, P. Spellman, R. Wilson, C. Sander, J. Weinstein, M. Meyerson, S. Gabriel, P. W. Laird, D. Haussler, G. Getz, L. Chin; TCGA Research Network, The somatic genomic landscape of glioblastoma. *Cell* **155**, 462–477 (2013).
24. W. A. Freije, F. E. Castro-Vargas, Z. Fang, S. Horvath, T. Cloughesy, L. M. Liau, P. S. Mischel, S. F. Nelson, Gene expression profiling of gliomas strongly predicts survival. *Cancer Res.* **64**, 6503–6510 (2004).
25. H. S. Phillips, S. Kharbanda, R. H. Chen, W. F. Forrest, R. H. Soriano, T. D. Wu, A. Misra, J. M. Nigro, H. Colman, L. Soroceanu, P. M. Williams, Z. Modrusan, B. G. Feuerstein, K. Aldape, Molecular subclasses of high-grade glioma predict prognosis, delineate a pattern of disease progression, and resemble stages in neurogenesis. *Cancer Cell* **9**, 157–173 (2006).
26. R. S. Brown, Zinc finger proteins: Getting a grip on RNA. *Curr. Opin. Struct. Biol.* **15**, 94–98 (2005).
27. B. M. Lunde, C. Moore, G. Varani, RNA-binding proteins: Modular design for efficient function. *Nat. Rev. Mol. Cell Biol.* **8**, 479–490 (2007).
28. J. Bonnet, C. Romier, L. Tora, D. Devys, Zinc-finger UBPs: Regulators of deubiquitylation. *Trends Biochem. Sci.* **33**, 369–375 (2008).
29. F. E. Reyes-Turcu, J. R. Horton, J. E. Mullally, A. Heroux, X. D. Cheng, K. D. Wilkinson, The ubiquitin binding domain ZnF UBP recognizes the C-terminal diglycine motif of unanchored ubiquitin. *Cell* **124**, 1197–1208 (2006).
30. D. Munoz-Espin, M. Serrano, Cellular senescence: From physiology to pathology. *Nat. Rev. Mol. Cell Biol.* **15**, 482–496 (2014).
31. C. Petropoulou, I. P. Trougakos, E. Kolettas, O. Toussaint, E. S. Gonos, Clusterin/apolipoprotein J is a novel biomarker of cellular senescence that does not affect the proliferative capacity of human diploid fibroblasts. *FEBS Lett.* **509**, 287–297 (2001).
32. O. Lyros, P. Rafiee, L. H. Nie, R. Medda, N. Jovanovic, J. Schmidt, A. Mackinnon, N. Venu, R. Shaker, Dickkopf-1, the Wnt antagonist, is induced by acidic pH and mediates epithelial cellular senescence in human reflux esophagitis. *Am. J. Physiol. Gastrointest. Liver Physiol.* **306**, G557–G574 (2014).
33. F. Mattiroli, J. H. A. Vissers, W. J. van Dijk, P. Ikpa, E. Citterio, W. Vermeulen, J. A. Marteijn, T. K. Sixma, RNF168 ubiquitinates K13-15 on H2A/H2AX to drive DNA damage signaling. *Cell* **150**, 1182–1195 (2012).
34. V. M. Weake, J. L. Workman, Histone ubiquitination: Triggering gene activity. *Mol. Cell* **29**, 653–663 (2008).
35. N. Mailand, S. Bekker-Jensen, H. Faustrup, F. Melander, J. Bartek, C. Lukas, J. Lukas, RNF8 ubiquitylates histones at DNA double-strand breaks and promotes assembly of repair proteins. *Cell* **131**, 887–900 (2007).
36. Z. Zhang, H. Yang, H. Wang, The histone H2A deubiquitinase USP16 interacts with HERC2 and fine-tunes cellular response to DNA damage. *J. Biol. Chem.* **289**, 32883–32894 (2014).
37. Y. Qian, B. Wang, A. Ma, L. Zhang, G. Xu, Q. Ding, T. Jing, L. Wu, Y. Liu, Z. Yang, Y. Liu, USP16 downregulation by carboxyl-terminal truncated HBx promotes the growth of hepatocellular carcinoma cells. *Sci. Rep.* **6**, 33039 (2016).
38. J. Ge, W. Yu, J. Li, H. Ma, P. Wang, Y. Zhou, Y. Wang, J. Zhang, G. Shi, USP16 regulates castration-resistant prostate cancer cell proliferation by deubiquitinating and stablizing c-Myc. *J. Exp. Clin. Cancer Res.* **40**, 59 (2021).
39. G. Xu, Z. Yang, Y. Ding, Y. Liu, L. Zhang, B. Wang, M. Tang, T. Jing, K. Jiao, X. Xu, Z. Chen, L. Xiang, C. Xu, Y. Fu, X. Zhao, W. Jin, Y. Liu, The deubiquitinase USP16 functions as an oncogenic factor in K-RAS-driven lung tumorigenesis. *Oncogene* **40**, 5482–5494 (2021).
40. J. C. Acosta, J. Gil, Senescence: A new weapon for cancer therapy. *Trends Cell Biol.* **22**, 211–219 (2012).
41. P. A. Perez-Mancera, A. R. J. Young, M. Narita, Inside and out: The activities of senescence in cancer. *Nat. Rev. Cancer* **14**, 547–558 (2014).
42. C. Nardella, J. G. Clohessy, A. Alimonti, P. P. Pandolfi, Pro-senescence therapy for cancer treatment. *Nat. Rev. Cancer* **11**, 503–511 (2011).
43. A. Ventura, D. G. Kirsch, M. E. McLaughlin, D. A. Tuveson, J. Grimm, L. Lintault, J. Newman, E. E. Reczek, R. Weissleder, T. Jacks, Restoration of p53 function leads to tumour regression in vivo. *Nature* **445**, 661–665 (2007).
44. W. Xue, L. Zender, C. Miething, R. A. Dickins, E. Hernando, V. Krizhanovsky, C. Cordon-Cardo, S. W. Lowe, Senescence and tumour clearance is triggered by p53 restoration in murine liver carcinomas. *Nature* **445**, 656–660 (2007).
45. H. Shiraha, K. Gupta, K. Drabik, A. Wells, Aging fibroblasts present reduced epidermal growth factor (EGF) responsiveness due to preferential loss of EGF receptors. *J. Biol. Chem.* **275**, 19343–19351 (2000).
46. Q. Liu, X. Xu, M. Zhao, Z. Wei, X. Li, X. Zhang, Z. Liu, Y. Gong, C. Shao, Berberine induces senescence of human glioblastoma cells by downregulating the EGFR-MEK-ERK signaling pathway. *Mol. Cancer Ther.* **14**, 355–363 (2015).
47. S. Zhang, B. S. Zhao, A. Zhou, K. Lin, S. Zheng, Z. Lu, Y. Chen, E. P. Sulman, K. Xie, O. Bögler, S. Majumder, C. He, S. Huang, m^6A demethylase ALKBH5 maintains tumorigenicity of glioblastoma stem-like cells by sustaining FOXM1 expression and cell proliferation program. *Cancer Cell* **31**, 591–606.e6 (2017).
48. A. Zhou, K. Lin, S. Zhang, Y. Chen, N. Zhang, J. Xue, Z. Wang, K. D. Aldape, K. Xie, J. R. Woodgett, S. Huang, Nuclear GSK3β promotes tumorigenesis by phosphorylating KDM1A and inducing its deubiquitylation by USP22. *Nat. Cell Biol.* **18**, 954–966 (2016).
49. H. Wen, Y. Li, Y. Xi, S. Jiang, S. Stratton, D. Peng, K. Tanaka, Y. Ren, Z. Xia, J. Wu, B. Li, M. C. Barton, W. Li, H. Li, X. Shi, ZMYND11 links histone H3.3K36me3 to transcription elongation and tumour suppression. *Nature* **508**, 263–268 (2014).
50. A. Zhou, K. Lin, S. Zhang, L. Ma, J. Xue, S.-A. Morris, K. D. Aldape, S. Huang, Gli1-induced deubiquitinase USP48 aids glioblastoma tumorigenesis by stabilizing Gli1. *EMBO Rep.* **18**, 1318–1330 (2017).

Acknowledgments: We thank A. Sutton (University of Texas MD Anderson Cancer Center) for editing our manuscript. We thank P. S. Mischel (Stanford University School of Medicine) for helpful suggestions and discussions. **Funding:** This work was supported by U.S. NIH grants R01NS101959, R01GM130838, R01NS117668, and P30CA016059 and by Paul M. Corman MD Chair in Cancer Research endowment fund. **Author contributions:** L.L., A.Z., and S.H. conceived the project and designed the research experiments. L.L., A.Z., F.L., Y.C., P.L., R.F., L.M., S.Z., L.W., J.L., and Y.W. performed the experiments. H.W., Y.C., and H.T.R. provided cell lines, reagents, and conceptual advice. L.L., A.Z., and S.H. wrote and revised the manuscript. S.H. supervised the study. All authors discussed the results and commented on the manuscript. **Competing interests:** The authors declare that they have no competing interests.

Data and materials availability: The microarray data of this study have been stored as NCBI GEO DataSets under accession number GSE186945. ChIP-seq data have been stored to NCBI GEO DataSets under accession number GSE207441. All data needed to evaluate the conclusions in the paper are present in the paper and/or the Supplementary Materials.

Submitted 7 December 2021
Accepted 18 August 2022
Published 5 October 2022
10.1126/sciadv.abn2571